Towards Mechanically Intelligent Reconfiguration via Origami Bifurcations

Chenying Liu, *Member, IEEE,* Liang He, *Member, IEEE,* Albert Williams, Perla Maiolino, *Member, IEEE,* and Zhong You

***Abstract*—Reconfigurability allows robots to create new morphologies to better match their environment or task. This ability is often viewed as a form of robotic intelligence. The process of reconfiguration is typically achieved either by mechatronic modules that disassemble and reassemble themselves, or by malleable bodies such as soft materials and linkage-like mechanisms with multiple degrees of freedom (DoFs). Despite these advances, the former approach can compromise robustness due to reconnections, while the latter often reduces controllability as the system's DoFs proliferate. To address these limitations, we introduce a novel reconfigurable robot based on thick-panel rigid origami and exploit kinematic bifurcations, branch points in the configuration space, to realise multiple configurations without module reconnections and without increasing overall DoF. In our framing, the bifurcation mechanism constitutes the element of mechanical intelligence that enables the intelligent behaviour of reconfiguration. As a proof-of-concept, we built a chain of interlinked rigid origami units that morphs among coil, wave-like, and triangular shapes, mimicking the morphology of a millipede. We also observe additional configurations due to compliant joint behaviour relative to the ideal model. Furthermore, the robot's dynamic performance and locomotion modes are explored. The work represents a further step towards real-world deployment of mechanically intelligent robots, illustrating the enabling role of bifurcation-guided reconfiguration.**

***Index Terms*—Reconfigurable robot, thick-panel origami, kinematic bifurcation, single-DoF design, mechanical intelligence.**

I. Introduction

RECONFIGURATION refers to the process where a system is arranged into different shapes [1]. For robots, reconfigurability enables transformations into task-appropriate morphology, thus better adapting to complex or changing environments [2]. Prior examples include end effectors that reconfigure for dexterous manipulation (e.g., elongatable fingers [3] and reconfigurable palms [4]) and locomotion systems that adapt geometry to terrain (e.g., variable-size wheels [5]).

Despite rapid progress, most, if not all, reconfigurable robots fall into two categories. Modular designs physically disassemble and reassemble mechatronic units to create new morphologies, offering broad reconfigurability but introducing reconnection overheads and potential misalignments [6]. In contrast, high-mobility mechanisms, such as linkages and malleable or soft bodies, achieve reconfiguration by increasing degrees of freedom (DoFs), which typically demand many actuators and complex control [4], [7]. Realising reconfiguration while simultaneously minimising reconnections and overall mobility remains challenging.

In this paper, we regard reconfigurability as a type of intelligence for robots. The term mechanical intelligence hence refers to the physical mechanism by which an intelligent behaviour is enabled, including but not limited to reconfiguration [8]. Origami structures, mechanical architectures inspired by paper folding, have become a popular physical substrate for implementing robotic intelligence. For instance, Bhovad et. al. [9] have shown that connected origami units can generate peristaltic locomotion using a single actuator, with functionality arising from structural multi-stability. Although the origami concept has been used in reconfigurable systems [10]–[12], its potential to achieve reconfiguration with minimal reconnections and low overall mobility remains underexplored.

To address the reconfiguration challenge and research gap, we use thick-panel origami, a special type of rigid origami architectures that accommodate finite facet thickness and operate with low mobility [13], [14]. Many such designs exhibit kinematic bifurcations: at specific singular states, the system increases its mobility instantaneously and bifurcates into different motion paths to transform its configuration. While these features of thick-panel origami have previously enabled dexterous manipulation with fewer actuators [15], here we extend the principle to whole-body reconfiguration. By exploiting bifurcations of a single-DoF mechanism, we realise multiple configurations without module reconnections and without increasing the system's overall mobility.

As a proof of concept, we construct a reconfigurable, single-DoF chain of interconnected, thick-panel origami units whose shape changes are primarily driven by kinematic bifurcations. The chain morphs among coil, wave-like, and triangular configurations (millipede-like morphologies). The underlying design principles and kinematic behaviours were analysed in our prior work [16], [17]. Here, we present the first physical prototype of this chain-based robot, integrating actuation and

This work was supported by the EPSRC Programme Grant "From Sensing to Collaboration" (EP/V000748/1) and a Junior Research Fellowship from Christ Church, University of Oxford. *(Corresponding authors: Chenying Liu.)*

The authors are affiliated with Department of Engineering Science, University of Oxford, Parks Road, Oxford OX1 3PJ, United Kingdom (e-mail: chenying.liu@eng.ox.ac.uk; liang.he@eng.ox.ac.uk; albert.t.b.williams@gmail.com; perla.maiolino@eng.ox.ac.uk; zhong.you@eng.ox.ac.uk).

C. Liu and P. Maiolino are also with the Oxford Robotics Institute, University of Oxford, 23 Banbury Road, Oxford OX2 6NN, United Kingdom

C. Liu and L. He are also with the Podium Institute for Sports Medicine and Technology, University of Oxford, Oxford OX3 7DQ, United Kingdom.

This article has Supplementary Material provided by the authors available at: https://drive.google.com/file/d/1c9YboAmE6MImxlSWHtqV8kRWywVqKP18/view?usp=sharing.

control to realise these morphologies. We further explore the robot dynamic performance, including joint-level fatigue, motion trajectories, and locomotion. Additional configurations have also been observed, which arise from joint compliance. We detail the implications of bifurcation-guided, mechanically intelligent design and sketch avenues for future work.

The remainder of the paper reviews reconfigurable systems and positions our approach in Section II. Section III describes the design of the origami chain and its actuation mechanism. Section IV details the fabrication and experimental setup. The results and analysis are presented in Section V. Finally, Section VI concludes with advantages, limitations, and future directions. The main contributions of the work are as follows.

1) Introduction of a novel reconfiguration strategy enabled by origami bifurcations, which is argued to be a manifestation of mechanical intelligence.
2) A single-DoF robot prototype that realises eight distinct morphologies (plus extra configurations arising from joint compliance) and requires no module reconnection.
3) Experimental characterisation of dynamic performance (motion trajectories, locomotion, joint-level fatigue) that demonstrates advantages relative to other reconfigurable robots and identifies priorities for future enhancement.

II. Related Work

A. Reconfigurable Robots

Reconfigurability is often framed as a facet of robotic intelligence, as it enables robots to adapt their morphologies for appropriate tasks. A substantial amount of work achieves reconfiguration via modular robots whose mechatronic units disassemble and reassemble to form chains or lattices [6], [18]–[21]. While powerful, repeated reconnection can introduce alignment errors and failure risks [22].

An alternative is to reconfigure without connectivity changes, using malleable bodies or high-DoF mechanisms. Examples include linkage-based morphing, which relies on inherent multi-DoF mechanisms, such as a 6R planar linkage of three DoFs to roll on the inclined surface [23] and a morphable palm using a 5R linkage to enhance interaction efficiency with grasped objects [4]. Additionally, malleable materials, such as soft materials with infinite DoFs, are employed in robots to enable transitions between functional modes [7], [24], [25].

B. Origami-Inspired Reconfigurable Robots

Origami, the ancient art of paper folding, can transform flat sheets into functional configurations. By combining rigid facets with compliant, rotary joints, origami-inspired designs have been a popular approach to reconfigurable robots.

One example keeps the conventional modular design, using origami facets as tiles that are interconnected via coupling mechanisms. For example, the Mori series, i.e., modular origami robots, can produce diverse structures from the same surface of polygons by activating different connections [10], [26]. Another route exploits the soft-bodied properties of origami structures similar to those in soft materials. By carefully designing the actuation mechanisms, structures such as the Kresling origami modules can change their morphologies to navigate through confined space [27], or bend and twist like a human arm [11]. Each module is controlled separately.

TABLE I
Representative Reconfiguration Approaches. OR=origami; Y=yes; N=no; RE=reconfiguration; H=high; L=low; M=medium.

Approach	RE	DoF	Material	Fatigue	Ref.
Modular design	Y	H	Mechatronic	RE wear	[21]
High-DoF	N	H	Link/elastomer	Elastomer	[4]
Rigid OR	N	L	Thin sheet	Joint	[30]
Non-rigid OR	N	M	Thin sheet	Facet/joint	[29]
This work	N	L	Thick sheet	Joint	N/A

Many of the above origami-inspired approaches exploit useful physical properties, but they still depend heavily on coordination and complex control to achieve reconfiguration, offering limited distinction from linkage- or soft-body reconfigurable robots. A route closer to mechanical intelligence is to manipulate joint states, for example, by switching mountain and valley assignments or selectively actuating folds via structural dynamics [8], [28]. These strategies reduce reconnections and can lower control complexity to some extent, although they still require fold-subset selection and state management.

C. Comparative Analysis and Gap

Common reconfiguration approaches are summarised in Table I. In general, a greater number of module reconnections and higher DoFs of a robot indicate enhanced reconfigurability. The modular design maximises configuration range but sacrifices its robustness. High-DoF systems avoid reconnection but often increase control complexity. The use of origami structures has offered good modularity, compliant but more controllable bodies, and, to some extent, improves the robustness and control efficiency. However, many designs assume origami to be zero-thickness (e.g., Miura fold) or non-rigid (e.g., Kresling, twisted tower). In practice, the former is limited to paper or thin materials while the later requires facet deformation, causing fatigue from repeated motions [29]. Both origami designs are heavily dependent on material properties. This motivates reconfigurable origami architectures that:

- realise multiple target configurations without changing connectivity while keeping DoFs minimal;
- are compatible with finite-thickness, rigid facets (not limited to paper or thin films); and
- keep facets essentially undeformed, so cyclic strains are localised to the joints, which are a small, replaceable fraction and can be made from fatigue-resistant materials.

We explore bifurcation-driven reconfiguration in thick-panel rigid origami as a route to mechanical intelligence. The structure achieves multiple morphologies without reconnection and without increasing overall DoF. The facets can be selected for stiff, finite-thickness sheets, while cyclic strains are carried by replaceable, fatigue-resistant joints.

III. Millipede-like Origami Robot Chain

This section summarises a case study of the millipede, followed by the working principle of an origami chain and its

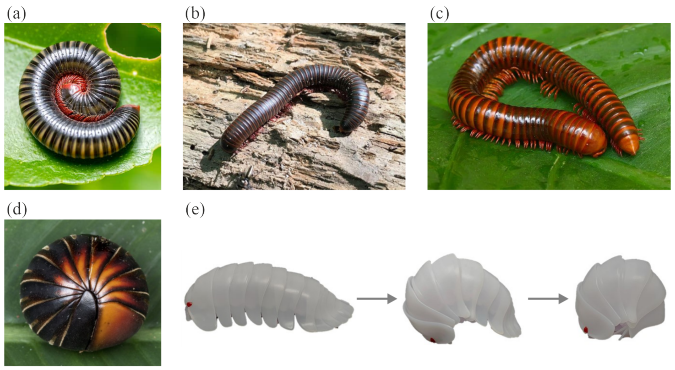

Fig. 1. Morphologies of a millipede, including **(a)** coil, **(b)** wave-like, and **(c)** triangular shapes. **(d)** Pill bug and **(e)** its toy version from Bandai Co., Ltd. Photos are adapted from [32]–[35].

actuation mechanism to mimic the millipede morphologies.

A. The Millipede and Its Morphology

From a biological perspective, while a millipede resembles worms in many ways, it is not a worm but an arthropod. The millipede's body segments are covered by stiff outer skins [31]. In response to danger, the millipede curls into a coil shape as shown in Fig. 1(a). The millipede also exhibits wavy and triangular shapes, as shown in Figs. 1(b) and 1(c).

Some in-depth research has been done on the peristaltic locomotion of millipedes [36]. Here, we focus on their curling mechanism and related configurations. As mentioned earlier, the millipede has a rigid exoskeleton, and we deduce that material deformation is not the primary cause of curling or other configurations. Since millipedes are very small, our previous work studied their biological relatives in the arthropod family, namely, the pill bug and the lobster [17]. The curling of the pill bug is reproduced in Fig. 1(d), along with its toy version in Fig. 1(e). Such animals share similar biological features to those of millipedes, which allow them to curl up. The results indicate that the curling mechanism essentially involves multiple body segments connected by rotational joints. It should be noted that these joints in millipedes do not exhibit perfect rotary motions. Instead, they permit deviations, and this kinematic redundancy contributes to wave-like and triangular configurations.

The reconfigurable nature and associated morphologies of millipedes make them adaptable to unstructured environments. Mimicking such behaviours in robots holds great potential for disaster search-and-rescue tasks. However, replicating the multi-DoF mechanism is not ideal, as it would require numerous actuators to drive each joint. To simplify the actuation and control system, we employ a single-DoF origami chain composed of interconnected rigid, thick-panel units. Despite its limited DoFs, the chain's bifurcated motion paths allow for a variety of configurations, as detailed below. This approach fundamentally differs from existing reconfiguration methods.

B. Working Principle of Reconfigurable Origami Chain

Figure 2(a) illustrates the origami pattern of the chain. On the 2D plane, the structure consists of identical equilateral

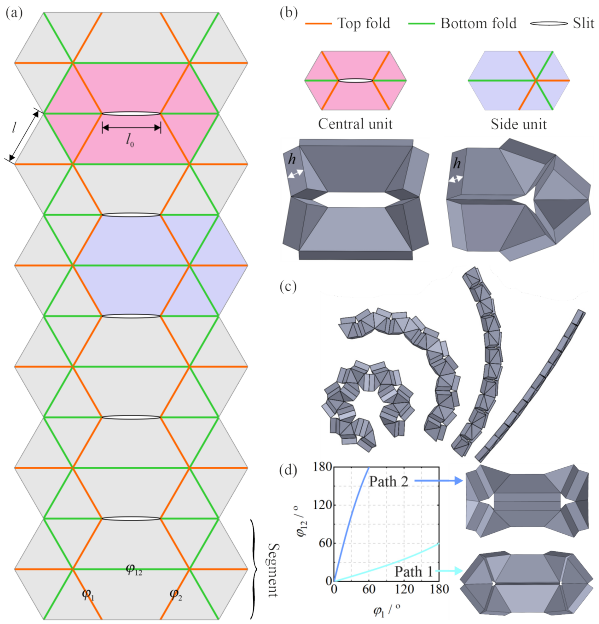

Fig. 2. Origami chain. **(a)** 2D pattern composed of identical equilateral triangles and isosceles trapezoids. The design parameters are also denoted. **(b)** Two types of constituent units and their 3D configurations. Each panel has an identical thickness h. **(c)** The curling process. **(d)** Bifurcated paths of a single segment, whose video is also available as Supplementary Material.

triangles and isosceles trapezoids. The folds are placed at the upper and lower surfaces of the chain, making it a thick-panel origami rather than the zero-thickness one. Only two types of units exist on the chain, namely the central unit and the side unit, as shown in Fig. 2(b). Each unit has six rigid panels with uniform thickness h. Their kinematic behaviours have been detailed in [17], both individually as a unit and collectively on the chain. Specifically, each unit possesses a single DoF with bifurcated motion paths. The bifurcation point is at the unfolded state where the structure is flat. The central unit has three possible motion paths, while each side unit has two. When interconnected to a chain, the single mobility characteristic is preserved due to shared folds. Bifurcation phenomena remain on the chain, and one motion path of the central unit is eliminated due to symmetry constraints.

The chain's motion is interesting. In particular, the chain can curl up into a coil shape, the side-view process of which is illustrated in Fig. 2(c). A pair of side units is defined as a segment, which further constructs a central unit with the adjacent segment. As denoted in Fig. 2(a), there are three shared folding, resulting in dihedral angles φ_1, φ_2, and φ_{12}. When a segment is mobile, it has two motion paths. The relationship among the shared dihedral angles are

$$\varphi_1 = \varphi_2 \tag{1}$$

when the segment is in path 1,

$$\tan\frac{\varphi_{12}}{2} = \frac{\sin\frac{\varphi_1}{2}}{2\cos\frac{\varphi_1}{2} + \sqrt{3}} \tag{2}$$

when the segment is in path 2,

$$\tan\frac{\varphi_{12}}{2} = \frac{\sin\frac{\varphi_1}{2}}{2\cos\frac{\varphi_1}{2} - \sqrt{3}} \tag{3}$$

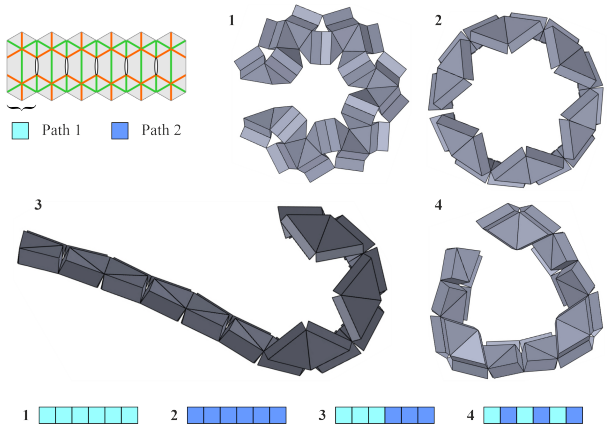

Fig. 3. Cross-sectional view of selected configurations. Curling, wave-like, and triangular morphologies can be obtained. They are all switchable at the kinematic bifurcations of the chain. Note that due to different curvatures, segments can look different even if they are in the same path. This is exemplified by configurations 1 and 3 where path 1 of each looks distinctive.

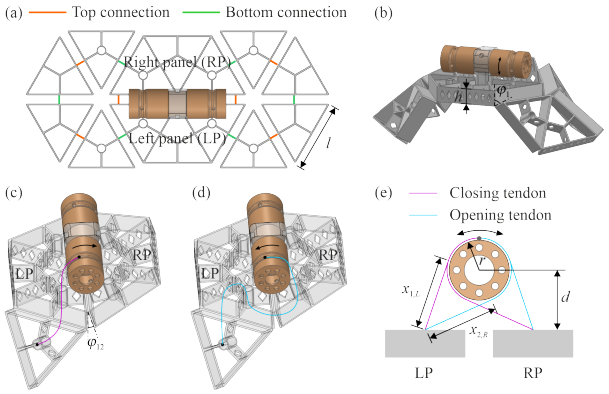

Fig. 4. Actuation design of a single segment. **(a)** Top view of the segment with a rotating axle. Note that the panel connections are upside-down from the original one in Fig. 2. **(b)** Side view of the segment in a semi-closed state. Two types of tendons are used to activate the segment. The arrangements of closing and opening tendons are exemplified in **(c)** and **(d)**, respectively. All four tendons connected to one side of the axle are illustrated in **(e)**.

whose plots and configurations are illustrated in Fig. 2(d).

The two bifurcated paths of a single segment form the foundation for reconfiguration. The number of morphologies on an n-segment chain is obtained by motion path permutation. Specifically, when n is odd, the number of motion paths is $2^{n-1}+2^{(n-1)/2}$. It becomes $2^{n-1}+2^{(n-2)/2}$ when n is even. Symmetric configurations are omitted. The six-segment chain shown in Fig. 2(a) can produce up to 32 distinct configurations, some of which are illustrated in Fig. 3. The associated motion path of each segment is also given, where path 1 is marked in light blue and path 2 is in dark blue. It is clear that the chain can not only curl up like the millipede's defensive mechanism, but also produce wave-like or triangular configurations.

All configurations can be switched from one to another at the bifurcation. The overall DoF is one at non-bifurcations.

C. Actuation Mechanism Design

The origami chain is taken as the backbone of a millipede-like robot. Due to friction and energy loss, it is not practical to activate the entire origami chain using only one actuator, despite being theoretically single-DoF. Instead, three segments are chosen to be actuated by a tendon-based system, and the other three are left with passive motions. Although multiple actuators are employed, their input signals remain identical without increasing control complexity.

The design of an actuated segment is illustrated in Fig. 4. Porous structures have been adopted on all panels to reduce self-weight. A rotating axle is attached to one trapezoid panel, which will be driven by a pair of motors on both sides. Tendon channels are left in some panels. Specifically, four sets of tendons are used to fold the segment from the flat state. The process is defined as the closing motion. Another four sets of tendons are used to reverse the motion and return the segment to the flat state, which is defined as the opening motion.

Note that for the actuated segment, the axle has physically blocked its path 2, leading to a decrease in the chain's possible configurations. The relationship between φ_1 and φ_{12} of such segments would only follow motion path 1 given in Eq. 2.

To illustrate the working principle of the actuation system, one closing tendon and one opening tendon, each with one end fixed to the left triangular panel, are presented in Figs. 4(c) and 4(d), respectively. The remaining tendons are arranged almost symmetrically to these examples. From their fixed points on the panels, each tendon follows its respective closing or opening path across different panels. The other end of each tendon is connected to the axle. Note that those with fixed ends on the right panel must pass underneath the axle and then join those starting from the left side to connect to the axle, as shown in Fig. 4(e), yielding a slight asymmetry.

When the axle rotates clockwise (CW), the closing tendon is pulled and the opening tendon is released. The segment is thus closed. When the axle rotates anticlockwise (ACW), the closing tendon is loosened and the opening tendon is pulled, causing the segment to open. The tendon length changes are first analysed kinematically as follows.

When the segment is in its flat state, the minimum required length (MRL) of each tendon, measured from the fixed point to the point just touching the axle, is defined below.

For the closing tendons, L_{1,L_0} and L_{1,R_0} denote the MRLs for the left and right sides, respectively.

$$L_{1,L_0}=\frac{\sqrt{3}}{3}l+2h+x_{1,L},\ L_{1,R_0}=\frac{\sqrt{3}}{3}l+2h+x_{1,R} \quad (4)$$

where l and h are given in Figs. 4(a) and 4(b), respectively. $x_{1,L}$ and $x_{1,R}$ are given by

$$x_{1,L}=x_{1,R}=\sqrt{d^2+\left(\frac{\sqrt{3}l}{6}\right)^2-r^2} \quad (5)$$

where d and r are illustrated in Fig. 4(e).

For the opening tendons, L_{2,L_0} and L_{2,R_0} are given as

$$L_{2,L_0}=\frac{2\sqrt{3}}{3}l+2h+x_{2,L},\ L_{2,L_0}=\frac{2\sqrt{3}}{3}l+2h+x_{2,R} \quad (6)$$

where $x_{2,L}=x_{2,R}=x_{1,L}$.

At a semi-folded configuration, the MRL for each tendon, whether starting from the left or right, and used for closing

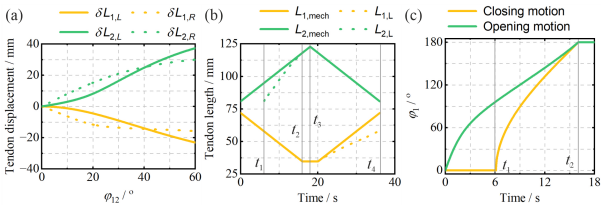

Fig. 5. Tendon length compatibility analysis. **(a)** Displacement of each tendon according to MRL analysis. **(b)** Actual tendon length throughout an actuation cycle taking slack into account. **(c)** Hysteresis loop of angle change, where $t_3 = t_2 + 2$ and the closing motion is mirrored.

or opening, are denoted by $L_{1,L}$, $L_{1,R}$, $L_{2,L}$, and $L_{2,R}$, respectively. Their mathematical representations are

$$\begin{aligned} L_{1,L} &= \frac{\sqrt{3}}{3} l \cos\frac{\varphi_1}{2} + 2h + x_{1,L} \\ L_{1,R} &= \frac{\sqrt{3}}{3} l \cos\frac{\varphi_1}{2} + 2h + x^*_{1,R} \end{aligned} \tag{7}$$

$$\begin{aligned} L_{2,L} &= \frac{2\sqrt{3}}{3} l + 2h + 2h(\sin\frac{\varphi_1}{2} + \sin\frac{\varphi_{12}}{2}) + x^*_{2,L} \\ L_{2,R} &= \frac{2\sqrt{3}}{3} l + 2h + 2h(\sin\frac{\varphi_1}{2} + \sin\frac{\varphi_{12}}{2}) + x_{2,R} \end{aligned} \tag{8}$$

where φ_1 and φ_{12} are depicted in Figs. 4(b) and 4(c), respectively. $x^*_{1,R}$ and $x^*_{2,L}$ need to be adjusted from their original values due to the slight difference between the tendon arrangements. Specifically, $x^*_{1,R} = x^*_{2,L}$, which is given by

$$x^*_{1,R} = \sqrt{(d - l\sin\varphi_{12})^2 + (\frac{\sqrt{3} l \cos\varphi_{12}}{6})^2 - r^2} \tag{9}$$

Given Eqs. 4 – 9, the required tendon displacements from the flat to semi-folded states are

$$\begin{aligned} \delta L_{1,L} &= L_{1,L} - L_{1,L_0} = L\frac{\sqrt{3}}{3} l(\cos\frac{\varphi_1}{2} - 1) \\ \delta L_{1,R} &= L_{1,R} - L_{1,R_0} = \delta L_{1,L} + x^*_{1,R} - x_{1,L} \\ \delta L_{2,L} &= L_{2,L} - L_{2,L_0} = \delta L_{2,R} + x^*_{2,L} - x_{2,L} \\ \delta L_{2,R} &= L_{2,R} - L_{2,R_0} = 2h(\sin\frac{\varphi_1}{2} + \sin\frac{\varphi_{12}}{2}) \end{aligned} \tag{10}$$

where $\delta L_{1,L}$ and $\delta L_{1,R}$ are negative, and their absolute values represent the pulled distances of the closing tendons. Similarly, $\delta L_{2,L}$ and $\delta L_{2,R}$ represent the released distances of the opening tendons. The displacements are plotted in Fig. 5(a), using the actual fabrication parameters provided in Section IV.

D. Analysis of Tendon Slack and Elasticity

As all tendons are pulled or released by the same mechanical distance via a common axle, which requires

$$\begin{aligned} \delta L_{1,L} = \delta L_{1,R},\ \delta L_{2,L} = \delta L_{2,R} \\ \delta L_{1,L} + \delta L_{2,L} = 0,\ \delta L_{1,R} + \delta L_{2,R} = 0 \end{aligned} \tag{11}$$

However, according to Fig. 5(a), the required displacements for each tendon are not kinematically compatible to satisfy Eq. 11. If we assume all tendons are under tension and perfectly inelastic, the actuated segment cannot move. Hence, to make the tendon displacements compatible with each other, some tendons might remain slack during part of the motion, and some might be stretched. Both slack and stretch influence how the segment behaves during actuation. Here, we analyse these effects from two perspectives, which are:

- The asymmetry between tendons with the same function, such as the left and right closing tendons.
- The dynamic behaviour of closing and opening tendons throughout an actuation cycle.

For the left and right closing tendons, consider the moment when both tendons are just entering tension and about to be pulled by the axle. The following equations can be used to describe their behaviour.

$$\begin{aligned} L_{\text{axle}} = \delta S_L - \delta L_{1,L} = \delta S_R - \delta L_{1,R} \\ F_L = k\delta S_L,\ F_R = k\delta S_R \end{aligned} \tag{12}$$

where L_{axle} is the tendon length rotated on the axle. δS_L and δS_R represent the stretch of the left and right closing tendons, respectively. F_L and F_R are the forces generated in each tendon, and k denotes the stiffness of the tendons.

As depicted in Fig. 5(a), $\delta L_{1,L}$ is larger than $\delta L_{1,R}$ when φ_{12} is less than $40°$. According to Eq. 12, we can deduce that, at the beginning of the closing movement, the left tendon has to be stretched more than the right tendon, which yields $\delta S_L > \delta S_R$. Consequently, a larger pulling force is generated in the left tendon. This uneven force distribution will result in the left side of the segment being in a more closed configuration than the right one. While this imbalance exists, the effect is minor, as the discrepancy between the geometric constraints of the left and right tendons is not significant.

With regard to the dynamic behaviour of the tendons, our analysis focuses on the left tendons. As shown in Fig. 5, the required released distance for the opening tendon is significantly larger than the pulled distance for the closing tendon. If both tendons are just in tension and the axle begins to rotate CW to close the segment, the released distance will be insufficient to meet the kinematic requirement, resulting in a back-driving force. To prevent this during closure and reduce torque demand on the axle, a predefined slack length L_{slack} is introduced to the closing tendon, allowing the opening tendon to release by the same distance before the closing tendon becomes taut. The slack can be carefully selected so that, during closure, the closing tendon starts slack and then gradually comes under tension. Meanwhile, the opening tendon remains slack throughout the motion and only approaches tension at the very end of closure. Hence, we have

$$L_{\text{slack}} = \delta L_{1,L} + \delta L_{1,R} \tag{13}$$

where the tendon length changes are taken at the end of closure configuration, at which point $\varphi_1 = 180°$ and $\varphi_{12} = 60°$.

Now let's analyse the tendon behaviour with the intentional slack. The mechanical lengths of the closing and opening tendons, $L_{1,\text{mech}}$ and $L_{2,\text{mech}}$ refer to the actual tendon lengths from their fixed points to the axle contact points.

At time $t = 0$ just before the axle starts to rotate CW, the initial mechanical lengths are given by

$$\begin{aligned} L_{1,\text{mech}}(t=0) &= L_{1,L_0} + L_{\text{slack}} \\ L_{2,\text{mech}}(t=0) &= L_{2,L_0} \end{aligned} \tag{14}$$

Assume that the axle is at a constant angular velocity ω to initiate the closure. The tendon length wound onto the axle is

$$L_{\text{axle}}(t) = r\omega t \tag{15}$$

During this closure phase, the mechanical lengths evolve as

$$\begin{aligned} L_{1,\text{mech}} &= L_{1,\text{mech}}(t=0) - L_{\text{axle}}(t) \\ L_{2,\text{mech}} &= L_{2,\text{mech}}(t=0) + L_{\text{axle}}(t) \end{aligned} \tag{16}$$

Slack in the closing tendon is taken up at t_1, obtained via Eqs. 13 and 15. Then, the closing tendon becomes taut. Given the small applied force, tendon stretch is neglected except for the overstretch stage. From now on, the closing tendon is in tension. At any time, $L_{1,\text{mech}}$ equals the MRL of the closing tendon, which is used to compute the opening tendon's MRL via Eqs. 7 and 8. If the corresponding length exceeds $L_{2,\text{mech}}$, a back-driving force is generated on the opening tendon.

At $t2$, $L_{1,\text{mech}}$ equals $L_{1,\text{mech}} = L_{1,L}$ ($\varphi_1 = 180°$), which indicates the segment is fully closed. This time point can be calculated accordingly. The axle continues CW rotation until $t3$. The closing tendon is overstretched, and $L_{1,\text{mech}}$ remains constant due to physical constraints. $L_{2,\text{mech}}$ continues to follow Eq. 16. The stretch of the closing tendon is

$$L_{\text{stretch}} = r\omega(t_3 - t_2) \tag{17}$$

At $t3$, the axle reverses direction and begins opening until $t4 = 2t_3$ to restore initial tendon lengths. Now we have

$$L_{2,\text{mech}} = L_{2,L_0} + L_{\text{axle}}(t = t_3) - L_{\text{axle}}(t - t_3) \tag{18}$$

At $t_3 + \Delta t_1$ when $L_{2,\text{mech}} = L_{2,L}(\varphi = 180°)$, the opening tendon becomes taut and begins to open the segment. Given our selection of the slack length, we can deduce $\Delta t_1 = t_3 - t_2$.

We also need to consider the viscoelastic release of the closing tendon from t_3 to $t_3 + \Delta t_2$, during which there is a non-negligible stretch while the axle no longer applies force. The behaviour is modelled as a Kelvin–Voigt element with stiffness k and damping η [37]. The time to release is governed by

$$k\delta S(t) + \eta \frac{d\delta S(t)}{dt} = 0 \tag{19}$$

with the initial condition $\delta S_L(t3) = L_{\text{stretch}}$, yielding

$$\delta S(t) = L_{\text{stretch}} e^{-\frac{k(t-t_3)}{\eta}},\ \Delta t_2 = \frac{\eta}{k} \ln\left(\frac{L_{\text{stretch}}}{L_{\text{threshold}}}\right) \tag{20}$$

where $L_{\text{threshold}}$ is taken as 1% of $L_{\text{threshold}}$.

Note that $L_{1,\text{mech}}$ will remain approximately equal to $L_{1,L}(\varphi = 180°)$ before it is fully released from stretch and the opening tendon is in tension. From that point, we have

$$L_{1,\text{mech}} = L_{1,L_0} + L_{\text{slack}} - L_{\text{axle}}(t = t_3) + L_{\text{axle}}(t - t_3) \tag{21}$$

The time evolution of $L_{1,\text{mech}}$ and $L_{2,\text{mech}}$ is shown in Fig. 5(b) using actual fabrication parameters in Section IV. Here $t_3 = t_2 + 2$ and the closing tendon is overstretched. When one tendon is taut, MRL values are also computed for the other to assess the presence of any back-driving force. The plots reveal that, due to the intentional slack, no back-driving force is generated during the actuation cycle, as the actual mechanical tendon lengths consistently exceed their MRL.

Based on the mechanical lengths of tendons that are in tension, φ_1 is inversely calculated from Eqs. 7 and 8. As shown in Fig. 5(c), the angle is plotted over time, with the opening period mirrored about $t = t_3$. A clear hysteresis loop is evident. We have also found that, without overstretch, which corresponds to the case when $t_3 = t_2$, the angle plot remains almost the same, except that the final plateau is removed. Note that from our analysis, hysteresis occurs only in actuated segments, as tendons are not connected to passive ones.

IV. Experimental Procedure

This section describes the fabrication of the robot. We then characterise the structure's joint fatigue and the robot's static configurations and actuated dynamic performance.

A. Fabrication Details

The key actuation components are shown in Fig. 6(a). The axle and rigid panels were 3D-printed in polylactic acid (PLA) using Creality Ender 3 with hollow structures to reduce weight. Panels were hand-assembled into a segment. As shown in Fig. 6(b), glass-fibre tapes were bonded to adjacent side walls to form foldable joints (hinge equivalents). Clear nylon fishing lines served as tendons for the actuated segments.

The parameters in Figs. 4 and 6 are as follows. Panel side length l and slit l_0 were 40 mm. Panel thickness h, axle height d, and radius r were 10 mm, 12 mm, and 8 mm, respectively.

Two MG90S servo motors, mounted symmetrically, drove the axle and were synchronised by a microcontroller (Arduino UNO) at an angular velocity ω of 0.291 rad/s. From the specifications, a single servo provides up to 171.2 N·mm torque, i.e., a pulling force of 21.4 N at an 8 mm arm. Each tendon set has an estimated stiffness $k = 7.08$ N/mm and a damping coefficient $\eta = 0.18$ Ns/mm. With two motors driving four tendon sets, the maximum tendon stretch is 1.5 mm.

In the final six-segment robot in Fig. 6(c), actuated segments are S_1, S_3, and S_5; S_2, S_4, and S_6 are passive. Because the actuated axles obstruct certain paths, the robot can achieve only eight configurations compared to 32 theoretically possible for a six-segment chain. For example, configurations 2 and 3 in Fig. 3 are not accessible with the current actuator layout.

We also printed entire origami chains in a single run. One model was fabricated in thermoplastic polyurethane (TPU) on Ultimaker 3 Extended. Thin TPU acted as a hinge and became rigid above 10 mm; detailed parameters are in our previous work [38], [39]. A PolyJet printer (Stratasys J735) produced a smaller version in VeroPureWhite™ with printed mechanical hinges. The PolyJet offers up to 14,μm resolution versus the Ultimaker's 0.2,mm, enabling miniaturisation. These prototypes are presented and compared in Section V.

B. Joint Level Fatigue Test

Because the chain follows the rigid-origami design, facet deformation is negligible and fatigue is expected to localise

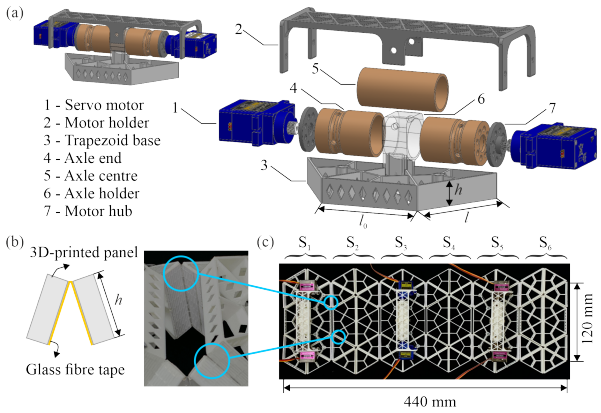

Fig. 6. Fabrication of a six-segment millipede-like robot. **(a)** Schematic design of the driving axle. **(b)** Fabrication of fold connections between panels. **(c)** Completed prototype of the robot with three actuated segments.

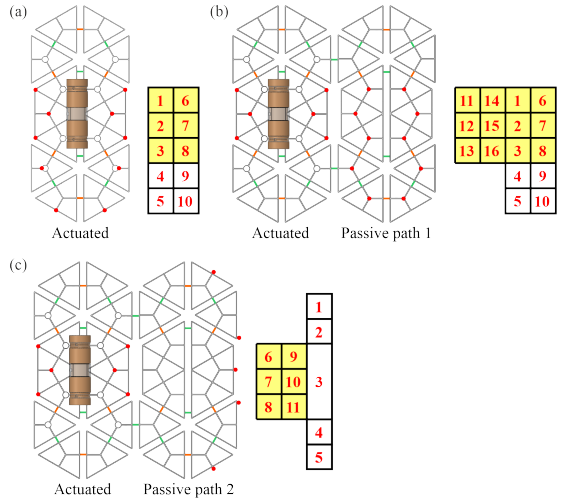

Fig. 7. Marker placement for **(a)** a single segment which only has path 1, **(b)** an actuated segment with a passive one in path 1, and **(c)** an actuated segment with a passive one in path 2.

at the foldable joints. To characterise joint durability under repeated folding, we used a Sarrus linkage to convert joint rotation into a linear stroke compatible with an Instron 5980 universal testing machine. Specimens are made of PLA rigid parts and glass-fibre tape as hinges. Tests were run under displacement control with a 20 mm amplitude at 1 mm/s for 1,000 cycles. The specimen details and a clip of cyclic motion is provided in the Supplementary Material.

C. Characterisation of the Actuated Prototypes

The entire robotic prototype was used to characterise the curling, wave-like, and triangular configurations. Single and double segments were actuated to evaluate their kinematic behaviours. The experimental setup is as follows.

The robotic prototype in Fig. 6(c) was used to validate its eight configurations. Motors were controlled synchronously for actuation. It should be noted that reconfigurable robots can be manually reconfigurable or self-reconfigurable. This work only focuses on the configurations themselves without considering the means of reconfiguration. Hence, the passive segments had to be manually switched into path 1 or path 2.

Additionally, single- and double-segment subsets of the six-segment system were tested to demonstrate and verify the underlying kinematic behaviour at a more manageable scale. Incremental validation of these smaller units provides evidence supporting the motion characteristics of the complete structure.

Specifically, two basic cases were used: (a) a single actuated segment, and (b) double segments where one is actuated and one is passive. Markers were affixed to multiple panels as illustrated in Fig. 7. Each marker is highlighted in red and numbered on the side. The single segment was only examined for its path 1, as shown in 7(a). For the double segments, path 1 of the passive segment was evaluated using the marker arrangement in Fig. 7(b). Path 2 was assessed according to Fig. 7(c). The different marker arrangements ensure that each path is achievable and the markers' positions can be recorded by the motion capture system (OptiTrack) without occlusion.

Markers with a yellow background were used to calculate the dihedral angles between adjacent trapezoid panels, i.e., $\varphi_{12-\text{actuated}}$, $\varphi_{12-\text{passive}}$, and $\varphi_{\text{actuated-passive}}$. Their relationship with φ_{12} and φ_1 on the origami chain is

$$\begin{aligned} \varphi_{12-\text{actuated}} &= \varphi_{12-\text{passive}} = \varphi_{12} \\ \tan\frac{\varphi_{\text{actuated-passive}}}{2} &= 2\cot\frac{\varphi_1}{2} \end{aligned} \tag{22}$$

where φ_1 and φ_{12} are obtained from Eqs. 2 and 3.

The distance between marker i and marker j is named $d_{i,\,j}$. Their theoretical values are given in the Supplementary Material with the marker's diameter d_0 taken into account.

Last but not least, the segments and the robotic prototype were also explored for locomotion strategies such as crawling and rolling. They were tested on a flat surface and a slope.

V. Results

A. Fatigue Resistance

The joint specimen completed 1,000 cycles with no observable cracks, delamination, or fraying at either the rigid facets or the glass-fibre tape joints. Hinge function and range of motion were maintained throughout. Fatigue studies on origami are limited. In Lee et al. [29], a non-rigid origami design, where both facets and joints deform, showed visible damage after 1,000 cycles, despite optimised fabrication parameters. This comparison suggests that rigid, thick-panel origami with foldable joints is a promising route to fatigue-resistant design, outperforming non-rigid counterparts.

B. Robot Configurations

The six-segment robot has demonstrated its configurations as shown in Fig. 8. Simulated models from SOLIDWORKS are also displayed for comparison, with the motion path of each segment indicated.

The curling motion is achieved in Fig. 8(a), replicating the behaviour of a millipede when disturbed as shown in Fig. 1(a). Figs. 8(e) and 8(h) give a closed-loop configuration which can be approximated to a triangle in Fig. 1(c). The rest of the configurations mimic the wave-like morphology of a crawling millipede in Fig. 1(b). The diverse morphologies greatly increase the reconfigurability of the robot.

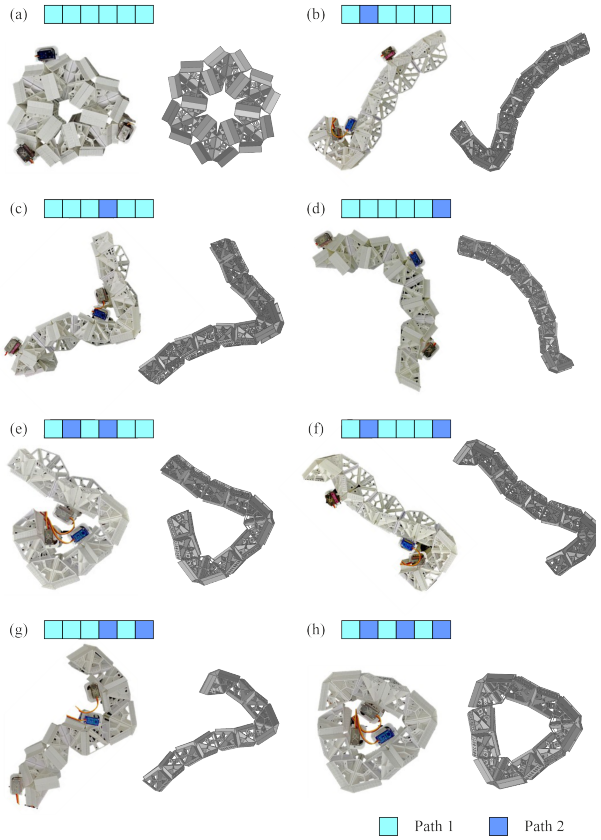

Fig. 8. Eight configurations of the robot in comparison with simulations.

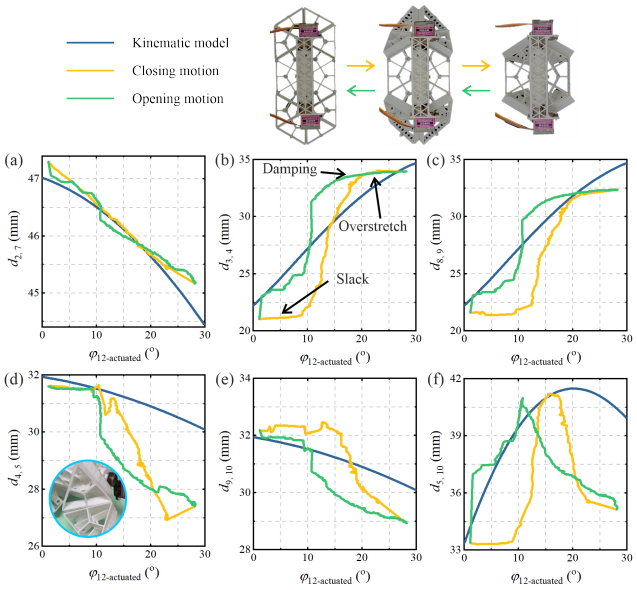

Fig. 9. Experimental results of the single segment in path 1 compared with the kinematic model. The segment's configurations from flat to folded states are illustrated. Note that the range of the vertical axis differs for each distance, making some of the errors seemingly bigger than others but actually not. The same note applies to Figs. 10 and 11.

C. Single Segment Behaviour

Experimental results of the single segment are given in Fig. 9. Kinematic predictions are also plotted for comparison.

In general, the motions match the kinematic model, albeit with some degree of deviation. On top of system errors in the motion capture system, the compliance of the folds, arising from the deformation and partial detachment of glass-fibre tapes, is deduced to have played a key role. As highlighted in Fig. 9(d), the tape-based fold was distorted and even detached slightly. Hence, its motion could deviate from ideal revolute joints which only have rotary motions. This can cause minor deformations such as twisting and stretching. In this case, the folded configuration can be influenced by external forces, such as friction and supporting forces from the ground. A small displacement at the joint can cause a big discrepancy in the dihedral angle and distance between adjacent panels.

As predicted by Eq. 12, the left side of the single segment closed more than the right side due to tendon elasticity and the resulting asymmetry. This effect is reflected in the differences between $d_{3,4}$ and $d_{8,9}$, where the former is on the left side and exhibits a slightly larger displacement over one actuation cycle. A similar trend is also observed between $d_{4,5}$ and $d_{9,10}$.

Hysteresis also occurs between the closing and opening motions. Fig. 5 shows the kinematic difference between the opening and closing tendons is the key factor. Specifically, $d_{2,7}$ is associated only with the opening tendon, which stays mostly slack throughout the cycle, hence little hysteresis. In contrast, other distances are directly controlled by the closing tendons or their associated motions, producing more pronounced hysteresis. In particular, for both $d_{3,4}$ and $d_{8,9}$ shown in Figs. 9(b) and 9(c), the displacement curves exhibit an initial plateau due to slack. At the final stage of closing, the tendon becomes overstretched due to panel blockage, resulting in minimal displacement between the markers.

Note that in Fig. 9(b), a longer plateau stage appears at the start of the opening motion, which was not predicted by our model. We attribute this phenomenon to a back-driving force from the closing tendon that resists the segment's opening. Although we have modelled the viscoelastic relaxation of the closing tendons to account for this effect, the tendon's damping ratio was relatively small (0.18 Ns/mm). In reality, the damping of the system can be significantly higher due to additional friction, such as that between the tendons and panels, and between the panels and the ground during opening. This likely results in a damping-like response during opening.

D. Double Segment Behaviour

Results for the double segments are shown in Figs. 10 and 11. The passive segment is in path 1 and path 2, respectively.

When in path 1, the experimental results of the passive segment align well with the theoretical model, as shown in Figs. 10(a) - 10(f). Little hysteresis exists, as no tendons are connected to the passive segment. The phenomenon further confirms that hysteresis arises from the tendon arrangement. When it comes to the relationship with the actuated segment, the angle change matches with the prediction as shown in Fig. 10(g). However, the marker distances have a much larger discrepancy, as evidenced by Figs. 10(h) and 10(i). The associated hinges are either only connected to opening tendons, which remain mostly slack, or left passive without any active tendons.

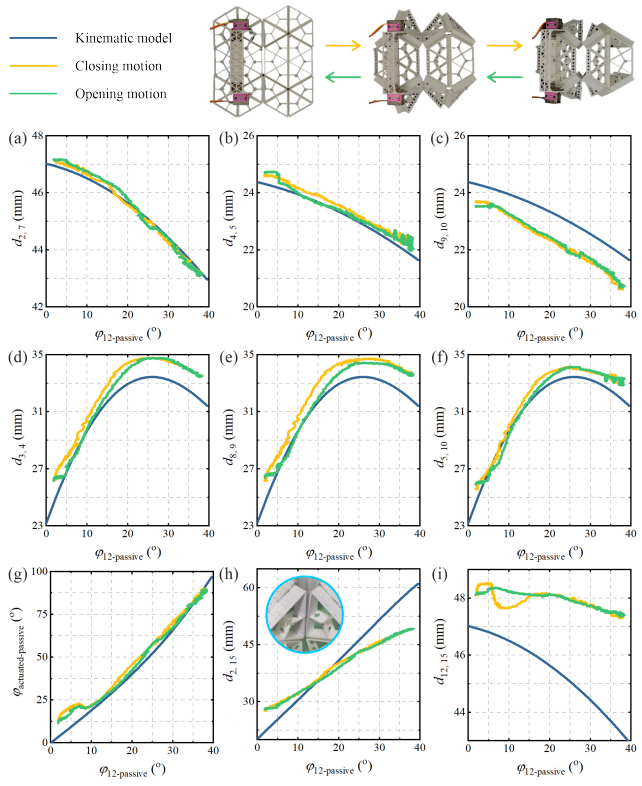

Fig. 10. Experimental results of double segments compared with the kinematic model. The passive segment is in path 1.

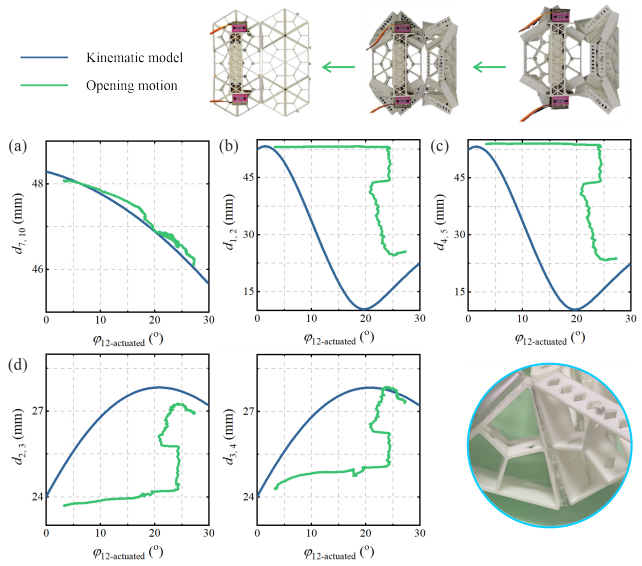

Fig. 11. Experimental results of double segments compared with the kinematic model. The passive segment is in path 2.

As analysed before for the single segment, Fig. 10(h) shows that the tape-based fold is stretched on one side, yielding motions beyond pure rotation. This phenomenon accounts for the discrepancy in the experimental trajectories.

When the passive segment is in path 2, only opening motions were evaluated. This is because a manual switch was required to access the path. As shown in Fig. 11(a), the panel distance on the actuated segment matches well

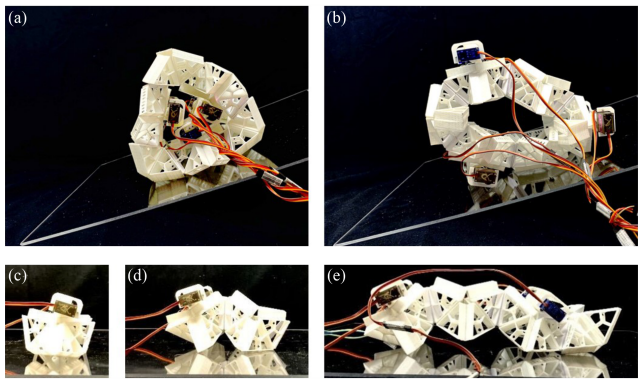

Fig. 12. Locomotion potential of actuated prototypes. **(a)** The curling and **(b)** triangular configurations roll down a slope. Crawling behaviours have been achieved on **(c)** a single segment, **(d)** double segments, and **(e)** four segments.

with the associated dihedral angle. A substantial discrepancy from the prediction is observed in Figs. 11(b) - 11(e), where only the starting and ending points are close to the model. This occurs because, when the passive segment is folded, friction and ground support forces resist its opening. Similar to the previous explanation, when the active segment gradually unfolds, the compliance of the tape-based folds allows for this kinematic incompatibility to persist until the active segment becomes more open. At that point, a sharp return to the original state is observed in the passive segment due to gravity.

E. Locomotion Potential

Although our focus is reconfiguration strategy, we briefly evaluated locomotion as shown in Fig. 12. The curling and triangular configurations enable rolling. Crawling-like motion is achievable with single, double, and four segments by driving the motors clockwise and anticlockwise in cycles, a video of which is available in the Supplementary Material. Hysteresis likely contributes to propulsion, and friction feet between segments and the ground could be added to improve efficiency. Current results use synchronous motor control, while locomotion performance could be tuned by sequencing the motors.

Additionally, with one or two segments, their motion follows path 1. With four segments, one end switches to path 2 without explicit control. This switching mechanism needs to be fully understood and may offer a route to self-reconfiguration.

F. Fully 3D-Printed Origami Model

A six-segment chain printed in TPU and a six-segment PolyJet model both form a closed circle as shown in as shown in Figs. 13(a) and 13(b), respectively, which are predicted by kinematics. The TPU version is three times larger, illustrating geometric scalability. A longer 18-segment PolyJet chain achieves spiral/helical shapes beyond theoretical predictions, as illustrated in Fig. 13(c). This is due to kinematic redundancy in the printed mechanical hinges, which allows motion beyond pure rotation and further enhances reconfigurability.

VI. Discussion and Conclusion

We demonstrate a bifurcation-driven strategy for reconfiguration, which was implemented on a millipede-like prototype

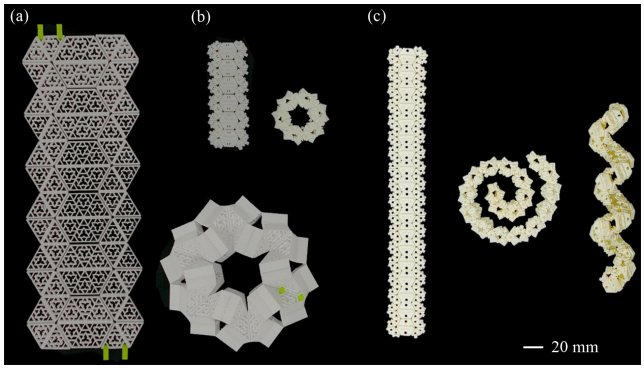

Fig. 13. Fully 3D-printed models. **(a)** TPU-based and **(b)** VeroPureWhite-based six-segment chains and their closed configurations. **(c)** VeroPureWhite-based long chain with spiral and twisting configurations.

with eight configurations. Unlike conventional modular approaches, our method requires no reassembly. It also leverages the bifurcation of a single-DoF system, simplifying coordination compared to those of high-DoF linkages or soft materials.

Compared with other origami-inspired reconfigurable robots, our design uses thick-panel, rigid origami chains in which facets remain undeformed and cyclic strains are localised to the joints. This widens the facet material choices beyond paper or thin films to thicker sheets, and shifts durability design to the hinges, where simple fatigue-resistant materials (e.g., glass-fibre tapes) can be used to sustain 1,000-cycle joint-level tests with no visible damage.

The robot chain exhibits eight configurations predicted by the kinematics, and we also observed additional variants attributable to joint compliance. Preliminary dynamics indicate hysteresis, which likely aids propulsion in crawling-like motion under synchronous drive. Rolling was also achieved in the curling and triangular forms. Together with bifurcation-guided shape change, these behaviours point towards mechanical intelligence, a useful behaviour arising from structure and intrinsic mechanics with minimal control overhead.

As a proof-of-concept, the current system is a medium-sized robot relying on manual selection at bifurcation, and factors like joint compliance are not included in the model. Future work will hence focus on the following areas.

First of all, although automatic switching is beyond this paper's scope, we identify viable routes such as encoding multi-stability and exploiting ground interaction to trigger bifurcation path changes. Such mechanisms could enable self-reconfiguration with minimal sensing and actuation.

Secondly, incorporating joint compliance and environmental forces into the model can improve motion prediction and control efficiency. These factors, together with kinematic bifurcations [40], [41], are not unique to thick-panel origami and have been observed in other mechanisms. We will complete the theory and extend it to other structures to broaden the reconfigurable robots' functionality.

Lastly, because the approach is geometry-driven, it is inherently scale-independent. At the microscale, it could enable reconfigurable tools for minimally invasive devices where compactness and repeatable switching are critical; at the meso scale, it can support reconfigurable interiors, assistive robots, and mobility aids; and at the macro scale, it can realise deployable and morphing structures such as space solar panels and shelters. Translating across scales will require appropriate hinge materials and actuation strategies.

ACKNOWLEDGMENTS

C.L. thanks Dr Peter Walter and Mr Cleveland Williams for prototyping suggestions, Dr Peihao Song for fatigue testing, and Profs Barbara Rossi and Jonathan Rossiter for reviewing her doctoral thesis, a chapter of which underpins this work.

REFERENCES

[1] A. Brunete, A. Ranganath, S. Segovia, J. P. De Frutos, M. Hernando, and E. Gambao, "Current trends in reconfigurable modular robots design," *International Journal of Advanced Robotic Systems*, vol. 14, no. 3, p. 1729881417710457, 2017.

[2] K. Støy, "Reconfigurable robots," *Springer Handbook of Computational Intelligence*, pp. 1407–1421, 2015.

[3] S. J. Yoon, M. Choi, B. Jeong, and Y.-L. Park, "Elongatable gripper fingers with integrated stretchable tactile sensors for underactuated grasping and dexterous manipulation," *IEEE Transactions on Robotics*, vol. 38, no. 4, pp. 2179–2193, 2022.

[4] Q. Lu, N. Baron, A. B. Clark, and N. Rojas, "Systematic object-invariant in-hand manipulation via reconfigurable underactuation: Introducing the ruth gripper," *The International Journal of Robotics Research*, vol. 40, no. 12-14, pp. 1402–1418, 2021.

[5] D.-Y. Lee, S.-R. Kim, J.-S. Kim, J.-J. Park, and K.-J. Cho, "Origami wheel transformer: A variable-diameter wheel drive robot using an origami structure," *Soft robotics*, vol. 4, no. 2, pp. 163–180, 2017.

[6] A. Castano, A. Behar, and P. M. Will, "The conro modules for reconfigurable robots," *IEEE/ASME transactions on mechatronics*, vol. 7, no. 4, pp. 403–409, 2002.

[7] D. S. Shah, J. P. Powers, L. G. Tilton, S. Kriegman, J. Bongard, and R. Kramer-Bottiglio, "A soft robot that adapts to environments through shape change," *Nature Machine Intelligence*, vol. 3, no. 1, pp. 51–59, 2021.

[8] T. Wang, C. Pierce, V. Kojouharov, B. Chong, K. Diaz, H. Lu, and D. I. Goldman, "Mechanical intelligence simplifies control in terrestrial limbless locomotion," *Science Robotics*, vol. 8, no. 85, p. eadi2243, 2023.

[9] P. Bhovad, J. Kaufmann, and S. Li, "Peristaltic locomotion without digital controllers: Exploiting multi-stability in origami to coordinate robotic motion," *Extreme Mechanics Letters*, vol. 32, p. 100552, 2019.

[10] C. H. Belke and J. Paik, "Mori: a modular origami robot," *IEEE/ASME Transactions on Mechatronics*, vol. 22, no. 5, pp. 2153–2164, 2017.

[11] S. Wu, Q. Ze, J. Dai, N. Udipi, G. H. Paulino, and R. Zhao, "Stretchable origami robotic arm with omnidirectional bending and twisting," *Proceedings of the National Academy of Sciences*, vol. 118, no. 36, p. e2110023118, 2021.

[12] J. Kaufmann, P. Bhovad, and S. Li, "Harnessing the multistability of kresling origami for reconfigurable articulation in soft robotic arms," *Soft Robotics*, vol. 9, no. 2, pp. 212–223, 2022.

[13] Y. Chen, R. Peng, and Z. You, "Origami of thick panels," *Science*, vol. 349, no. 6246, pp. 396–400, 2015.

[14] S. V. Georgakopoulos, C. L. Zekios, A. Sattar-Kaddour, M. Hamza, A. Biswas, B. Clark, C. Ynchausti, L. L. Howell, S. P. Magleby, and R. J. Lang, "Origami antennas," *IEEE Open Journal of Antennas and Propagation*, vol. 2, pp. 1020–1043, 2021.

[15] C. Liu, L. He, S. Wang, A. Williams, Z. You, and P. Maiolino, "Exploring kinematic bifurcations and hinge compliance for in-hand manipulation: How could thick-panel origami contribute?" *Advanced Intelligent Systems*, p. 2300691, 2024.

[16] C. Liu, F. Yang, P. Maiolino, and Z. You, "Morphing surfaces inspired by thick-panel origami," *International Journal of Mechanical Sciences*, p. 109976, 2025.

[17] C. Liu, Z. You, and P. Maiolino, "Kinematics of an origami inspired millipede robot," in *International Design Engineering Technical Conferences and Computers and Information in Engineering Conference*, vol. 86281. American Society of Mechanical Engineers, 2022, p. V007T07A062.

[18] J. Seo, J. Paik, and M. Yim, "Modular reconfigurable robotics," *Annual Review of Control, Robotics, and Autonomous Systems*, vol. 2, pp. 63–88, 2019.
[19] G. Liang, D. Wu, Y. Tu, and T. L. Lam, "Decoding modular reconfigurable robots: A survey on mechanisms and design," *The International Journal of Robotics Research*, vol. 44, no. 5, pp. 740–767, 2025.
[20] M. Yim, D. G. Duff, and K. D. Roufas, "Polybot: a modular reconfigurable robot," in *Proceedings 2000 ICRA. millennium conference. IEEE international conference on robotics and automation. Symposia proceedings (Cat. No. 00CH37065)*, vol. 1. IEEE, 2000, pp. 514–520.
[21] L. Zhao, Y. Wu, W. Yan, W. Zhan, X. Huang, J. Booth, A. Mehta, K. Bekris, R. Kramer-Bottiglio, and D. Balkcom, "Starblocks: Soft actuated self-connecting blocks for building deformable lattice structures," *IEEE Robotics and Automation Letters*, 2023.
[22] M. Yao, C. H. Belke, H. Cui, and J. Paik, "A reconfiguration strategy for modular robots using origami folding," *The International Journal of Robotics Research*, vol. 38, no. 1, pp. 73–89, 2019.
[23] C. Liu, O. Edwards, K. Althoefer, K. Zhang, and H. Godaba, "An electro-pneumatic shape morphing rolling robot with variable locomotion modes," in *2022 IEEE 5th International Conference on Soft Robotics (RoboSoft)*. IEEE, 2022, pp. 715–721.
[24] R. Baines, S. K. Patiballa, J. Booth, L. Ramirez, T. Sipple, A. Garcia, F. Fish, and R. Kramer-Bottiglio, "Multi-environment robotic transitions through adaptive morphogenesis," *Nature*, vol. 610, no. 7931, pp. 283–289, 2022.
[25] H. Gu, Q. Boehler, H. Cui, E. Secchi, G. Savorana, C. De Marco, S. Gervasoni, Q. Peyron, T.-Y. Huang, S. Pane *et al.*, "Magnetic cilia carpets with programmable metachronal waves," *Nature communications*, vol. 11, no. 1, p. 2637, 2020.
[26] C. H. Belke, K. Holdcroft, A. Sigrist, and J. Paik, "Morphological flexibility in robotic systems through physical polygon meshing," *Nature Machine Intelligence*, pp. 1–7, 2023.
[27] Q. Ze, S. Wu, J. Nishikawa, J. Dai, Y. Sun, S. Leanza, C. Zemelka, L. S. Novelino, G. H. Paulino, and R. R. Zhao, "Soft robotic origami crawler," *Science advances*, vol. 8, no. 13, p. eabm7834, 2022.
[28] C. Liu, S. J. Wohlever, M. B. Ou, T. Padir, and S. M. Felton, "Shake and take: Fast transformation of an origami gripper," *IEEE Transactions on Robotics*, vol. 38, no. 1, pp. 491–506, 2021.
[29] K. Lee, Y. Wang, and C. Zheng, "Twister hand: Underactuated robotic gripper inspired by origami twisted tower," *IEEE Transactions on Robotics*, vol. 36, no. 2, pp. 488–500, 2020.
[30] C. Wang, H. Guo, R. Liu, Z. Deng, Y. Chen, and Z. You, "Reconfigurable origami-inspired multistable metamorphous structures," *Science Advances*, vol. 10, no. 22, p. eadk8662, 2024.
[31] S. P. Hopkin, H. J. Read *et al.*, *The biology of millipedes.*, 1992.
[32] O. Northwest Pest Control, "What you need to know about millipede control: Millipede prevention," Jul 2020. [Online]. Available: https://www.callnorthwest.com/2020/07/what-you-need-to-know-about-millipede-control/
[33] O. Innovative Pest Control, "The secret to effective centipede & millipede control for your home," Oct 2020. [Online]. Available: https://www.ipcpest.com/blog/2020/october/the-secret-to-effective-centipede-millipede-cont/
[34] O. Native Pest Management, "Centipede & millipede identification in florida," Dec 2023. [Online]. Available: https://www.nativepestmanagement.com/pest-library/centipedes-and-millipedes
[35] K. Lanier, "Meet the roly poly (aka pill bug) & learn its roles in the garden," Jul 2017. [Online]. Available: https://www.hobbyfarms.com/roly-poly-pill-bug-garden-roles/
[36] A. Garcia, G. Krummel, and S. Priya, "Fundamental understanding of millipede morphology and locomotion dynamics," *Bioinspiration & Biomimetics*, vol. 16, no. 2, p. 026003, 2020.
[37] R. Lewandowski and B. Chorążyczewski, "Identification of the parameters of the kelvin–voigt and the maxwell fractional models, used to modeling of viscoelastic dampers," *Computers & structures*, vol. 88, no. 1-2, pp. 1–17, 2010.
[38] C. Liu, P. Maiolino, Y. Yang, and Z. You, "Hybrid soft-rigid deployable structure inspired by thick-panel origami," in *International Design Engineering Technical Conferences and Computers and Information in Engineering Conference*, vol. 83990. American Society of Mechanical Engineers, 2020, p. V010T10A080.
[39] C. Liu, P. Maiolino, and Z. You, "A 3d-printable robotic gripper based on thick panel origami," *Frontiers in Robotics and AI*, vol. 8, p. 730227, 2021.
[40] Y. Chen and Z. You, "Two-fold symmetrical 6r foldable frame and its bifurcations," *International Journal of Solids and Structures*, vol. 46, no. 25-26, pp. 4504–4514, 2009.
[41] Z. Tang, H. Feng, and J. S. Dai, "Computation of kinematic paths and bifurcation points for multi-degree-of-freedom mechanisms with singular value decomposition," *Mechanism and Machine Theory*, vol. 213, p. 106047, 2025.

Biography Section

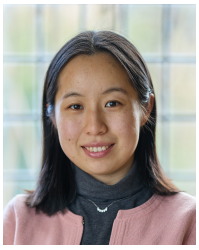

Chenying Liu (Member, IEEE) is currently a Junior Research Fellow at Christ Church and an Associate Member of Faculty in the Department of Engineering Science, University of Oxford. She earned her B.Eng. from Beihang University (2019) and her Ph.D. from the Special Structures Group and Soft Robotics Lab at the University of Oxford (2024). then stayed at the same institution and spent just over a year as a Postdoctoral Researcher in the Healthcare Biorobotics Lab at the Podium Institute for Sports Medicine and Technology. Her recent work focuses on advanced structures and materials for robotics and related fields.

Liang He (Member, IEEE) is an Associate Professor in the Department of Engineering Science, University of Oxford, and an Official Fellow of Kellogg College. He directs the Healthcare Biorobotics Lab at the Oxford Institute of Biomedical Engineering and is core faculty of the Podium Institute for Sports Medicine and Technology. He received a Ph.D. in soft robotics from Imperial College London in 2021. Durin his postdoctoral position at the Oxford Robotics Institute, he worked on the Embodied Intelligence Programme, developing soft-sensing robotic skin for human–robot interaction. His research includes soft robotics, biosensors, haptics and virtual reality, wearable robotics, and embodied AI for healthcare and biomedical applications, with recent work translating soft robotic innovations into medical training, rehabilitation, and injury prevention.

Albert Williams obtained the M.Eng. degree in Engineering Science from the University of Oxford in 2024 and was a member of Lady Margaret Hall. During his undergraduate studies, he worked with Dr Chenying Liu and Prof Zhong You in the Special Structures Group via the Engineering Undergraduate Research Opportunities Programme (EUROP), funded by the Department of Engineering Science. He is interested in structures and fluid mechanics, which led him to complete his Master's dissertation on the redevelopment of a high-speed wind tunnel, before returning to the Oxford Thermofluids Institute as a Research Engineer.

Perla Maiolino (Member, IEEE) received the B.Eng. in software engineering (2003), M.Eng. in robotics and automation (2006), and Ph.D. in robotics (2010) from the University of Genoa, Italy. She then joined the Mechatronic and Control Laboratory, University of Genoa as a Research Fellow, working on distributed tactile sensors to give robots a "sense of touch." She was a Post-Doctoral Researcher at the Biologically Inspired Robotics Lab, University of Cambridge, where she developed an interest in soft robotics and worked on soft robot sensing and perception. In September 2018, she joined the Oxford Robotics Institute and is now an Associate Professor in the Department of Engineering Science, University of Oxford, where she established the Soft Robotics Lab.

Zhong You is a Professor of Engineering Science in the Department of Engineering Science at the University of Oxford. He obtained his BS from Shanghai Jiaotong University, MS from Dalian University of Technology, and PhD from Cambridge University. His research focuses on the design and development of deployable structures, which are unconventional structures capable of significant shape changes. He has published numerous ground-breaking research papers in prestigious journals and has led the creation of minimally invasive medical devices and consumer products. His work was selected for the Science Day Exhibition at Buckingham Palace, organised by the Royal Society. His current research interests include origami and origami-based metamaterials and robots.